Available online at www.sciencedirect.com

ScienceDirect

Geochimica et Cosmochimica Acta 314 (2021) 1–15

Geochimica et Cosmochimica Acta

www.elsevier.com/locate/gca

Co-precipitation induces changes to iron and carbon chemistry and spatial distribution at the nanometer scale

Angela R. Possinger [a,1], Michael J. Zachman [b,2], James J. Dynes [c], Tom Z. Regier [c], Lena F. Kourkoutis [b,d], Johannes Lehmann [a,e,f,*]

[a] School of Integrative Plant Science, Section of Soil and Crop Sciences, Cornell University, USA
[b] School of Applied and Engineering Physics, Cornell University, USA
[c] Canadian Light Source, Saskatoon, SK, USA
[d] Kavli Institute at Cornell for Nanoscale Science, Cornell University, USA
[e] Cornell Atkinson Center for Sustainability, Cornell University, USA
[f] Institute for Advanced Studies, Technical University Munich, Garching, Germany

Received 31 March 2021; accepted in revised form 1 September 2021; Available online 8 September 2021

Abstract

Association of organic matter (OM) with mineral phases via co-precipitation is expected to be a widespread process in environments with high OM input and frequent mineral dissolution and re-precipitation. In contrast to surface area-limited adsorption processes, co-precipitation may allow for greater carbon (C) accumulation. However, the potential sub-micrometer scale structural and compositional differences that affect the bioavailability of co-precipitated C are largely unknown. In this study, we used a combination of high-resolution analytical electron microscopy and bulk spectroscopy to probe interactions between a mineral phase (ferrihydrite, nominally $Fe_2O_3 \bullet 0.5H_2O$) and organic soil-derived water-extractable OM (WEOM). In co-precipitated WEOM-Fe, nanometer-scale scanning transmission electron microscopy with electron energy loss spectroscopy (STEM-EELS) revealed increased Fe(II) and less Fe aggregation relative to adsorbed WEOM-Fe. Spatially distinct lower- and higher-energy C regions were detected in both adsorbed and co-precipitated WEOM-Fe. In co-precipitates, lower-energy aromatic and/or substituted aromatic C was spatially associated with reduced Fe(II), but higher-energy oxidized C was enriched at the oxidized Fe(III) interface. Therefore, we show that co-precipitation does not constitute a non-specific physical encapsulation of C that only affects Fe chemistry and spatial distribution, but may cause a bi-directional set of reactions that lead to spatial separation and transformation of both Fe and C forms. In particular, we propose that abiotic redox reactions between Fe and C via substituted aromatic groups (e.g., hydroquinones) play a role in creating distinct co-precipitate composition, with potential implications for its mineralization.

Keywords: Co-precipitation; Adsorption; Soil organic matter; Electron energy loss spectroscopy

1. INTRODUCTION

The potential for soil to act as a carbon (C) reservoir is limited by the environmental drivers of soil organic matter (SOM) accumulation, including interactions between SOM and soil minerals (Deng and Dixon, 2002; Schmidt et al., 2011; Lehmann and Kleber, 2015). The spatial and chemical complexity of SOM motivates the need to account for

* Corresponding author at: School of Integrative Plant Science, Section of Soil and Crop Sciences, Cornell University, USA.
E-mail address: CL273@cornell.edu (J. Lehmann).
[1] Current address: CUNY Advanced Science Research Center at the Graduate Center, City University of New York, New York, NY 10031, USA; Cary Institute of Ecosystem Studies, Millbrook, NY 12545, USA.
[2] Current address: Center for Nanophase Materials Sciences, Oak Ridge National Laboratory.

https://doi.org/10.1016/j.gca.2021.09.003
0016-7037/

non-equilibrium SOM stabilization processes, such as co-precipitation of soluble organic matter (OM) with newly-formed minerals in the soil solution (Kleber et al., 2015). Co-precipitation is a pathway of organo-mineral interaction that may allow for greater C accumulation than would be expected based on surface coverage alone. In the environment, OM-mineral co-precipitation is an especially relevant process in wetlands, rice paddies, hydric soils, or other zones of fluctuating anaerobic and aerobic conditions with abundant OM input (Chen et al., 2014). Co-precipitates can also be found in generally well-drained soils with microsites of O_2 depletion or fluctuating redox conditions, suggesting that the process may be common across terrestrial and aquatic ecosystems (Thompson et al., 2006; Collignon et al., 2012). As such, OM-mineral co-precipitates could be an important contribution to overall soil C stocks, and their properties are relevant for describing soil C persistence.

Mineral surface adsorption of OM and co-precipitation processes are expected to differ in their spatial and chemical composition. Co-precipitation with organic compounds has been linked to disruption of mineral structure and slowed crystallization, largely shown through experiments using ferrihydrite (nominally $Fe_2O_3 \bullet 0.5H_2O$), both with model C compounds (Mikutta et al., 2010; Mikutta, 2011) and natural OM (Vilge-Ritter et al., 1999; Henneberry et al., 2012). Similarly, increased Fe-organic bond formation has been demonstrated for co-precipitation compared to adsorption (Chen et al., 2014; Chen et al., 2016). These structural changes in organo-mineral associations may have relevance for microbial bioavailabity and redox transformations (Shimizu et al., 2013; Eusterhues et al., 2014; Mikutta et al., 2014; Ginn et al., 2017). Additionally, co-precipitation of mixed soluble Fe(II)/Fe(III) phases has shown to increase in the presence of Fe(II) (Henneberry et al., 2012; Fritzche et al., 2015), and co-precipitation has also been shown to induce Fe reduction in model systems (Mikutta, 2011). However, the presence of a reduced Fe phase after co-precipitation of natural OM with Fe (III) has been rarely detected, even across a range of C:Fe ratios, with either no detection of Fe(II) or no analysis of the Fe redox state (Vilge-Ritter et al., 1999; Chen et al., 2014; Chen et al., 2016). Consequently, though changes to mineral structure have become an accepted characteristic of OM-Fe co-precipitates, uncertainty still exists in the degree and nature of changes to Fe redox speciation. Additionally, structural changes are largely assessed through bulk characterization (e.g., X-ray diffraction), and nanometer-scale statistical spatial analysis of Fe distribution as a result of co-precipitation vs. adsorption is lacking.

The potential for physical occlusion of OM via co-precipitation with relatively little change compared to its original composition suggests that, on average, co-precipitated OM may be less altered from the precursor OM relative to adsorption, with implications for the stability and reactivity of co-precipitated mineral phases (Eusterhues et al., 2011; Euesterhues et al., 2014; Kleber et al., 2015). While co-precipitated OM may be more similar to source OM overall, selective incorporation of C functional groups in co-precipitates compared to source OM has been detected. However, the C form preferentially retained varies widely. For instance, experiments with bulk spectroscopic characterization of natural OM-ferrihydrite co-precipitates have shown both an increase (Chen et al., 2014) and decrease (Chen et al., 2016) in aromatic C, and an increase (Eusterhues et al., 2011; Henneberry et al., 2012) and decrease (Chen et al., 2014) in polysaccharide C. Additionally, microspectroscopic imaging (e.g., scanning transmission X-ray microscopy with X-ray absorption near edge structure, STXM-XANES) with $\sim$ 40–50 nm spatial resolution has shown divergent spatial distribution of OM, with some studies identifying complete intermixing of C and Fe phases and others patchy distribution of OM in co-precipitates (Henneberry et al., 2012; Chen et al., 2014). Previous imaging and spectroscopy approaches may be limited by spatial and chemical resolution, particularly for minerals with single nanometer-scale structure (e.g., ferrihydrite) (Schwertmann and Taylor, 1989). Due to these divergent views on alteration of OM forms with co-precipitation, differences in composition and spatial distribution between adsorbed and co-precipitated OM remain largely unresolved. The question underpins the assumption of divergent bioavailability, ultimately driving the C accumulation potential and persistence of co-precipitated OM.

To provide new understanding of the OM-Fe interaction processes distinct to co-precipitation, high-resolution visualization of spatial and chemical co-precipitate properties is needed. Scanning transmission electron microscopy with electron energy loss spectroscopy (STEM-EELS) is one approach for high-resolution structural and chemical analysis. This approach enables mapping of Fe and C speciation at single-digit nanometer (nm) spatial resolution, providing a means to identify local ($<$10 nm-scale) changes in co-precipitate composition. Additionally, STEM-EELS under cryogenic conditions (cryo-STEM-EELS) enhances analysis of Fe and C speciation by increasing potential spatial and spectral resolution for damage-sensitive elements, especially C (Kourkoutis et al., 2012; Miot et al., 2014).

Here, we applied STEM-EELS and cryo-STEM-EELS to describe the structural and chemical characteristics of water-extractable OM (WEOM)-Fe co-precipitates in comparison to adsorption complexes at the nanometer scale. Specifically, our aim was to compare (1) Fe spatial distribution and aggregation, (2) the presence of reduced Fe(II), (3) changes to C composition and spatial distribution of C forms, and (4) spatial association of C forms with Fe. Additionally, we contextualized high-resolution measurements using bulk X-ray absorption spectroscopy (XAS) approaches commonly used for OM and Fe minerals.

2. METHODS

2.1. Experiment overview

This study used water-extractable organic matter (WEOM) derived from organic horizons of forest soils as a source of OM for co-precipitation and adsorption experiments with ferrihydrite (nominally $Fe_2O_3 \bullet 0.5H_2O$). Co-precipitation treatments were prepared by addition of WEOM to dissolved Fe(III) followed by increase in pH

and precipitation of a WEOM-Fe co-precipitated solid phase. In contrast, adsorption treatments were prepared by addition of WEOM to previously precipitated, solid-phase ferrihydrite in suspension. To assess spatial elemental distribution, changes to Fe and C composition, and spatial association between Fe and C forms, high-resolution analytical STEM-EELS was paired with bulk characterization of total C (by combustion), bulk C and Fe K-edge XANES, and bulk Fe K-edge extended X-ray absorption fine structure (EXAFS).

2.2. Water-Extractable Organic Matter (WEOM) preparation

Water-extractable OM was prepared from organic horizons collected from upland forested Spodosols (Tunbridge-Lyman-Becket Series) in Watershed 3 (hydrological reference watershed) of the Hubbard Brook Experimental Forest (North Woodstock, NH). Organic horizon (Oa) soils were collected from three replicate profiles within < 20 m distance at two locations: Site 1 (43.955533°N, −71.718826°W), characterized by deep (~1 m), well-expressed Spodosol soil profiles, and Site 2 (43.956998 °N, −71.717241 °W), characterized by shallow-to-bedrock soil profiles (Possinger et al., 2020a). Sites 1 and 2 correspond to "typical" and "E" podzols, respectively, following nomenclature used in Bailey et al. (2014). Dominant forest vegetation at the sites is described in Possinger et al. (2020a). At Site 1, no coniferous tree species were identified in the 314 m^2 sampling area. At Site 2, coniferous basal area increased to 35%. However, for both locations, yellow birch (*Betula alleghaniensis*) occupied the most basal area of any individual species.

Water-extractable OM was derived as described in Possinger et al. (2020a). In brief, organic soil (Oa horizon) was composited from three replicate horizons at both Site 1 and Site 2. Water extractions (1:1 soil:water ratio, filtered to 0.45 μm) were stored at 4–9 °C until used for characterization analysis and co-precipitation and adsorption experiments. Total OC content was determined for the WEOM extracts using a Shimadzu TOC-$V_{CPH/CPN}$ instrument (Shimadzu Corportation, Kyoto, Japan) in a 1% hydrochloric acid (HCl) matrix. Total OC of WEOM extracts were determined to be 700 mg C L^{-1} WEOM for Site 1 and 469 mg C L^{-1} for Site 2.

2.3. Co-precipitation and adsorption sample preparation

Ferrihydrite (nominally Fe_2O_3•$0.5H_2O$) was prepared as described in Possinger et al. (2020b). In brief, Fe(III) nitrate (0.005 M) was titrated by addition of base (0.05 M KOH) to pH 7 (low-concentration modification of Schwertmann and Cornell, 2000) and purified by dialysis (1000 dalton molecular weight cut-off). For co-precipitates, WEOM was added at a 10:1 molar C:Fe ratio (determined based on TOC measurements described above) for both WEOM sources (i.e., from Sites 1 and 2) prior to titration (n = 4 synthesis replicates). This C:Fe ratio was selected based on C accumulation in adsorbed and co-precipitated C:Fe complexes investigated by Chen et al. (2014), wherein increasing initial C contents did not appreciably increase C accumulation above 10:1 C:Fe for adsorption.

WEOM-Fe adsorption complexes (n = 4 synthesis replicates) were prepared by addition of WEOM after precipitation of ferrihydrite at a 10:1 molar C:Fe ratio. For Fe K-edge XAS of Site 2 WEOM, n = 1 synthesis replicates were generated. The WEOM-ferrihydrite suspensions were shaken overnight in Teflon® centrifuge tubes to prevent adsorption to the container surfaces, followed by dialysis as described above. Fresh co-precipitate and adsorption WEOM-Fe samples were prepared prior to each analysis to limit crystallization artifacts. Samples were stored in water suspension at 4–9 °C for < 2 weeks before imaging and spectroscopy to minimize artifacts resulting from freeze or air-drying. For bulk C composition analysis, samples were shipped (~3-day) cool and refrigerated for an additional 2 weeks prior to C K-edge XANES analysis. For imaging and spectroscopy, all synthesis replicates were equally pooled and mixed in suspension. Prior to deposition of co-precipitate and adsorption suspensions for imaging, ~2 mL of suspension was centrifuged at 13,000 rpm for 10 minutes, followed by immediate resuspension in 0.5 mL Nanopure™ water to increase sample concentration and C signal yield.

2.4. Bulk characterization

2.4.1. Total carbon

Co-precipitate and adsorption complex solids were collected by filtration through 0.45 μm-pore GFF syringe filters, which were air-dried and analyzed for total C and N using a Carlo-Erba NC2500 elemental analyzer (CE Instruments Ltd, Wigan, UK), with adjustments for GFF filter weight and background (filter < 0.07 %C). Total C values were compared statistically using the two-sided Wilcoxon Rank Sum Test with base R (v. 4.0.2) (R Core Team, 2019) in RStudio (v. 1.1.423) (RStudio Team, 2015).

2.4.2. Iron K-edge X-ray Absorption Spectroscopy (XAS)

Iron XAS data were obtained at the Cornell High Energy Synchrotron Source (CHESS) F3 beamline (hard-bend magnet source with silicon (111) monochromator and silicon drift detector). Detailed beamline information and standard synthesis methods are described in Inagaki et al. (2020) and Possinger et al. (2020a). Samples (ferrihydrite without added WEOM and WEOM-Fe co-precipitates and adsorption solids) were prepared for XAS measurements by thin-layer deposition of a 60-μL suspension on 1-mil polyimide (Kapton®) tape. Fluorescence yield was measured (2–5 scans per sample) using the following dwell times and energy step sizes: 1–2 s and <0.005 keV for the pre-edge (6.912–7.092 keV), 2 s and 0.001 keV for the XANES region (7.093–7.143 keV), 5 s and variable energy step for the EXAFS region (7.144–7.637 keV).

Iron K-edge XANES analysis methods were modified from Inagaki et al. (2020) and Possinger et al. (2020a). In brief, Fe K-edge XANES spectra were processed using Athena v. 0.9.26 (Ravel and Newville, 2005). Normalized fluorescence yield (μ(E)) was used to determine white line and energy positions of the μ(E) pre-edge centroid. The first

derivative of normalized fluorescence yield, hereafter referred to as dx/dμ(E), was computed and the E_0 (edge position inflection point) was calculated as the maximum of dx/dμ(E). The energy position of the pre-edge feature in the dx/dμ(E) spectrum can shift to lower energies as a result of increasing Fe(II) and/or Fe-organic complex content (Fe 1s-4p transition-like character as a result of 3d-4p mixing with ligands) (Westre et al., 1997; Prietzel et al., 2007). Therefore, we used the dx/dμ(E) centroid in combination with spectral shifts associated with Fe(II) to tease apart XANES spectral features in standard compounds with variable Fe(II) and/or Fe-organic complex content. The relative intensity at ~ 7117–7120 eV in dx/dμ(E) (associated with the 1s-4s transition and increasing Fe(II) content) (Berry et al., 2003) was estimated using a four-Gaussian function curve fitting approach modified from Inagaki et al. (2020). Further details are included in Supplementary Methods A1.1.

The Fe K-edge EXAFS region was also used to qualitatively compare Fe-organic bonding in co-precipitated and adsorbed WEOM-Fe samples. The EXAFS forward Fourier transform (K-space) was computed for the 2–11 $Å^{-1}$ wavenumber range and plotted as k^2 (standards) or k^3 (samples)-weighted spectra following Chen et al. (2014) in Athena (Ravel and Newville, 2005). For samples, the inverse Fourier transform (R-space) or k^3-weighted K-space spectra was computed using the radial distance range of 1–3 Å.

2.4.3. Carbon K-edge XANES

Carbon K-edge X-ray absorption spectroscopy measurements were conducted at the Canadian Light Source (CLS) spherical grating monochromator (SGM) beamline. Information on the beamline and data collection procedures are described in Possinger et al. (2020a). In brief, co-precipitate and adsorption samples in suspension (~60 μL) were drop-cast and air-dried on Au-coated silicon wafers. Carbon partial fluorescence yield (PFY) scans (60 s scans, 32 for samples and 10 for standards) were measured using a silicon drift detector placed at 90 degrees to the incident beam in the plane of polarization in order to minimize scattering. The measurements were collected using a 50 × 50 μm incident beam size and normalized to the PFY scattering signal from a clean wafer.

Spectrum normalization and flattening procedures were performed in Athena v. 0.9.26 (Ravel and Newville, 2005), with the edge step set to 1. A deconvolution modeling approach was used for C K-edge XANES that fits 8 Gaussian functions to energy positions defined by multiple previous standard organic compound XANES studies (Solomon et al., 2009; Heymann et al., 2011). Non-negative Gaussian functions (G1-G8) were defined with the parameters: (1) square root of peak height, (2) peak center, and (3) peak full-width half-maximum (FWHM) (Hestrin et al., 2019), with peak centers allowed to float within 0.2 eV energy for G1-G7 and 0.1 eV for G8 and peak FWHM allowed to float by 0.4 eV for all functions (Supplementary Table A4.1). The model was fit for samples and verified with standard compounds (Supplementary Tables A4.2-A4.3) in Fityk v. 0.9.8 (Wojdyr, 2010) using the Levenberg-Marquardt algorithm with 1000 maximum iterations to minimize the maximum sum of squared residuals (MSSR). Models were accepted if $R^2 > 0.98$.

2.5. High resolution imaging and spectroscopy (STEM-EELS)

2.5.1. STEM-EELS data collection

Element distribution and Fe spatial clustering were analyzed with STEM-EELS for co-precipitated and adsorbed WEOM-Fe using WEOM from both sites. Additionally, C and Fe speciation were determined with high spatial resolution (<5 nm) for co-precipitated and adsorbed Site 2 WEOM-Fe using cryogenic STEM-EELS. Samples were prepared by drop-casting ~ 3 μL of each suspension directly on a Cu TEM grid (400-mesh) without a C film. Co-precipitate and adsorption sample droplets were spatially separated on the same grid, allowing for characterization of both treatments during one microscope session, thereby minimizing changes in experimental conditions between measurements. Imaging and spectroscopy data collection was conducted on an aberration-corrected FEI Titan Themis S/TEM instrument (FEI Company, Hillsboro, OR) equipped with a Gatan GIF Quantum 965 spectrometer (Gatan Inc., Pleasanton, CA) operated at 120 kV. For cryogenic STEM-EELS, used to determine Fe and C speciation, the samples were maintained at approximately −180 °C with spectrometer aperture and monochromator settings adjusted to improve spectral resolution (~0.5 eV) while maintaining a moderate beam current (0.025–0.16 nA). For all measurements, acquisition parameters are described in Supplementary Table A4.4. To assess elemental distribution, Fe aggregation, and Fe and C fine structure, 2D EELS maps were collected ranging in magnification from 225 kx to 2500 kx for the C K-edge (270–320 eV) and Fe $L_{2,3}$–edge (700–730 eV) (collected simulataneously). Additionally, N K-edge (380–430 eV) and O K-edge (500–540 eV) spectra were collected for Site 1 WEOM-Fe samples at room temperature.

2.5.2. Cryo-STEM-EELS beam damage assessment

Systematic differences in C and Fe STEM-EELS spectra as a function of dose and sample type were used to assess changes to the potentially beam-sensitive C and Fe constituents under cryogenic conditions (see Supplementary Methods A1.2, Supplementary Figs. A3.1-A3.3, Supplementary Table A4.5). In brief, differences between the sample types (adsorbed vs. co-precipitated) and across different regions of the same sample accounted for variation in Fe and C composition, rather than systematic trends related to dose (Supplementary Figs. A3.1-A3.3). While we note that the EELS signal in the oxidized (e.g., carboxylic C) region may be more sensitive to damage than other C components, beam damage artifacts did not explain C compositional or spatial trends (Supplementary Figs. A3.1-A3.2, Supplementary Results and Discussion A2.1).

2.5.3. Elemental spatial distribution and clustering

Elemental EELS maps of Fe, C, N, and O in Site 1 WEOM-Fe samples and Fe and C in Site 2 WEOM-Fe

samples were used to assess spatial relationships between elements and the spatial aggregation patterns of Fe. Data processing and spatial statistics (Ripley's K(t) and Moran's I) are described in Supplementary Methods A1.3-A1.4 and Supplementary Figs. A3.4-A3.5.

2.5.4. EELS carbon and iron fine structure

Changes in C and Fe spectral features associated with chemical composition (i.e., fine structure) for high-magnification adsorption and co-precipitation samples (WEOM from Site 2 only) were statistically evaluated with multivariate curve resolution (MCR) (Mundy et al., 2014; Baek et al., 2016; Zachman et al., 2018), performed using the pyMCR Python package (Camp, 2019). The number of putative components was set to 2 and initial regions for spectrum guesses were selected close to and more distant from higher-Fe structures. Spectroscopic images recorded at > 1.3 Mx magnification and with sufficient sample area were selected for MCR analysis.

Spatial correlations among Fe and C forms identified with MCR were performed using R in RStudio (RStudio Team, 2015; R Core Team, 2019). For each MCR output image, non-sample area (vacuum) was manually filtered to avoid inflation of correlation estimates and intensity was normalized to maximum = 1 (see Supplementary Methods A1.3). Pixel intensity correlations among C and Fe components, total C, and total Fe were determined using Spearman Rank correlation. In addition, a line profile of relative component intensity across a region of the co-precipitate image with the highest spatial resolution (measurement "i" in Supplementary Table A4.4) was collected in ImageJ v. 2.0.0 (Schneider et al., 2012) to assess finer-resolution shifts in component distribution.

3. RESULTS

3.1. Bulk characterization

3.1.1. Total carbon

No significant differences were found in the total C content of the co-precipitation or adsorption samples derived from Site 1 or Site 2 WEOM (Wilcoxon Rank Sum test, all $p > 0.3$) (Supplementary Fig. A3.6). Due to the lack of significant differences in the total C content between WEOM sources, the total C data for co-precipitation or adsorption were pooled across WEOM types (Supplementary Fig. A3.6). Both co-precipitated and adsorbed WEOM-Fe interacted with and thereby accumulated C, ranging from approximately 16–70 %C by weight (mean 34 ± 14 s.d. %C). The median total C followed an overall trend of lower C for adsorption in comparison to co-precipitation samples. However, the difference between co-precipitated and adsorbed total C was not statistically significant (Wilcoxon Rank Sum test, $p = 0.40$).

3.1.2. Iron K-edge X-ray absorption spectroscopy

For both co-precipitated and adsorbed WEOM-Fe, no change in the 7117–7120 eV intensity of the first derivative spectrum (a metric of increasing Fe(II)) was detected relative to the oxidized ferrihydrite standards (Table 1, Supplementary Fig. A3.7). A lower-energy shift (approximately −0.3 eV) in the first-derivative (dx/dμE) pre-edge centroid was detected for co-precipitated WEOM-Fe only, with less than ± 0.06 eV shift detected for adsorption (Table 1). The shift was not detected in the edge inflection point (E_0) energy, but an approximately −0.5–1 eV shift in white line energy position was detected for co-precipitated WEOM-Fe (Table 1). Due to the lack of change in 7120 eV intensity, we attribute these shifts to increased Fe-organic bonding in the co-precipitate sample. Fe K-edge XANES measurements were also similar for Site 1 and Site 2 WEOM sources (Table 1).

The Fe-K edge EXAFS Fourier transform spectra (K-space) showed a slight increase in Fe-organic bonding for co-precipitated WEOM-Fe, with a subtle decrease in amplitude of the oscillation at 7.5 $Å^{-1}$ compared to adsorption samples and reference ferrihydrite, corresponding to high-shell backscatter due to Fe-organic bonding (Chen et al., 2014) (Supplementary Figs. A3.8-A3.9). However, these changes were not reflected in the inverse Fourier transform (R-space), which predominantly showed features associated with Fe-O and Fe-Fe bonds (Supplementary Fig. A3.8). Taken together, the similar magnitude of pre-edge centroid shifts to Fe-organic standards and the slight changes in the EXAFS K-space amplitude suggest that bulk Fe chemistry of co-precipitated Fe-WEOM showed greater Fe-organic bonding than for adsorption (Supplementary Fig. A3.10).

3.1.3. Carbon K-edge X-ray absorption spectroscopy

Carbon K-edge XANES spectra were similar between both WEOM sources in both overall shape and fine structure (Possinger et al., 2020a) and deconvolution results (Fig. 1, Supplementary Fig. A3.11, Supplementary Table A4.2). Due to the lack of compositional differences between WEOM sources and normalization of preparation based on WEOM C concentration, results are hereafter pooled with respect to WEOM source (see Supplementary Results and Discussion A2.2). The largest contribution to the WEOM C K-edge XANES signal was derived from the aromatic region, with the sum of functions (Gaussian functions 1–4) resulting in 45 ± 3 s.d.% (average of WEOM sources) of the total Gaussian function area of the XANES spectrum (Fig. 1, Supplementary Fig. A3.11, Supplementary Table A4.2).

Carbon K-edge XANES spectra for adsorbed vs. co-precipitated WEOM were similar overall, with only a slight increase in carboxylic acid C in adsorbed WEOM (Fig. 1, Supplementary Fig. A3.11). This similarity is reflected in deconvolution results, which do not show appreciable differences between adsorbed and co-precipitated samples (Fig. 1, Supplementary Table A4.2). However, the contribution of the aromatic signal was reduced by approximately two-fold for both adsorbed and co-precipitated samples compared to the initial WEOM source (Fig. 1, Supplementary Fig. A3.11, Supplementary Table A4.2). Additionally, alkyl C decreased with co-precipitated and adsorbed WEOM-Fe compared to source WEOM, with an associated proportional increase in oxidized C (e.g., carboxylic and O-alkyl/carbonyl functional groups).

Table 1
Iron (Fe) K-edge X-ray absorption near-edge structure (XANES) results for adsorption and co-precipitation samples prepared using water-extractable organic matter (WEOM) from Site 2 and Site 1. µE = fluorescence spectrum, E_0 = edge inflection point, and dx/d(µE) = the first derivative of µE.

	WEOM sourced from Site 2				WEOM sourced from Site 1			
	Adsorbed		Co-precipitated		Adsorbed		Co-precipitated	
	Ferrihydrite reference	WEOM-Fe	Ferrihydrite reference	WEOM-Fe	Ferrihydrite reference	WEOM-Fe	Ferrihydrite reference	WEOM-Fe
µE pre-edge centroid (eV)	7114.0	7114.0	7114.0	7114.0	7114.5	7114.8	7114.5	7114.5
µE white line (eV)	7132.0	7132.0	7133.0	7132.0	7132.8	7132.3	7133.0	7132.5
E_0 (eV)	7127.0	7127.0	7127.0	7127.0	7127.3	7127.0	7127.3	7127.3
dx/d(µE) 7120 eV area (%)	2.0	1.6	5.3	1.6	7.7	9.9	8.0	3.2
dx/d(µE) pre-edge centroid (eV)	7112.3	7112.4	7112.1	7111.8	7113.2	7113.2	7113.3	7113.0
dx/d(µE) pre-edge centroid shift (eV)	NA*	+0.06	NA	−0.31	NA	+0.03	NA	−0.23

*NA = not applicable. Pre-edge centroid shift is determined relative to oxidized Fe (ferrihydrite) reference position.

3.2. High resolution imaging and spectroscopy (STEM-EELS)

3.2.1. STEM-EELS overview mapping

Lower-magnification (<910 kx-magnification) overview annular dark field (ADF) STEM images and EELS Fe and C elemental maps showed a different spatial arrangement between the co-precipitation and adsorption Fe-WEOM samples (Fig. 2). In general, Fe with adsorbed WEOM was more spatially clustered while co-precipitated Fe with WEOM was more evenly mixed.

3.2.2. Elemental spatial distribution

On average, Fe and C were approximately 4 times more spatially separated (i.e., negative Spearman's ρ) for adsorbed compared to co-precipitated WEOM-Fe (Wilcoxon Rank Sum $p = 0.07$, W = 12) (Table 2). For both adsorbed and co-precipitated WEOM-Fe, Fe and O were spatially co-located (i.e., positive Spearman's ρ) (Table 2). Nitrogen (N) was neither spatially separate nor co-located with either Fe or C (i.e., Spearman's ρ close to zero) (Table 2).

3.2.3. Iron distribution and clustering

Consistent with the spatial separation between Fe and C, Ripley's K(t) metric (see Supplementary Methods A1.4) showed overall more Fe clustering with greater distances (i.e., larger clusters) for adsorbed WEOM-Fe in the majority of maps used for Fe spatial statistics (Fig. 3). There was variability in Fe clustering within co-precipitates, but overall, Fe was more randomly distributed or clustered at shorter distances (i.e., in smaller clusters) (Fig. 3). Further, the median Moran's I statistic (Fe spatial autocorrelation) was higher for adsorption vs. co-precipitation (Wilcoxon Rank Sum $p < 0.05$, W = 49) (Fig. 3).

3.2.4. Multivariate Curve Resolution (MCR)

All EELS measurements contained an Fe component associated with oxidized Fe(III) (Supplementary Fig. A3.12) (fixed at 710.5 eV in this study) (Gloter et al., 2004). For co-precipitated WEOM-Fe (n = 5 EELS measurements), a shoulder at lower energy (~709.0 eV) associated with increasing Fe(II) was detected in the primary Fe component relative to adsorbed WEOM-Fe (n = 2 EELS measurements) (Supplementary Fig. A3.12). Further, a secondary reduced Fe(II) component with an L_3-edge position shifted to ~ 709.0 eV was detected for 2 out of 5 co-precipitated WEOM-Fe images (Supplementary Fig. A3.12). For adsorbed WEOM-Fe, either no secondary component or an Fe(III) component associated with thicker sample area were detected.

For both adsorbed and co-precipitated WEOM-Fe, MCR-resolved C K-edge spectra generally showed components corresponding to higher- and lower-energy C forms (Fig. 4). The lower-energy C component had stronger contributions from features at ~ 285–286.5 and 287–287.5 eV, putatively associated with aromatic or substituted aromatic C = C, and C-H transitions, respectively (Solomon et al., 2009; Zachman et al., 2018). The loss of oxidized features

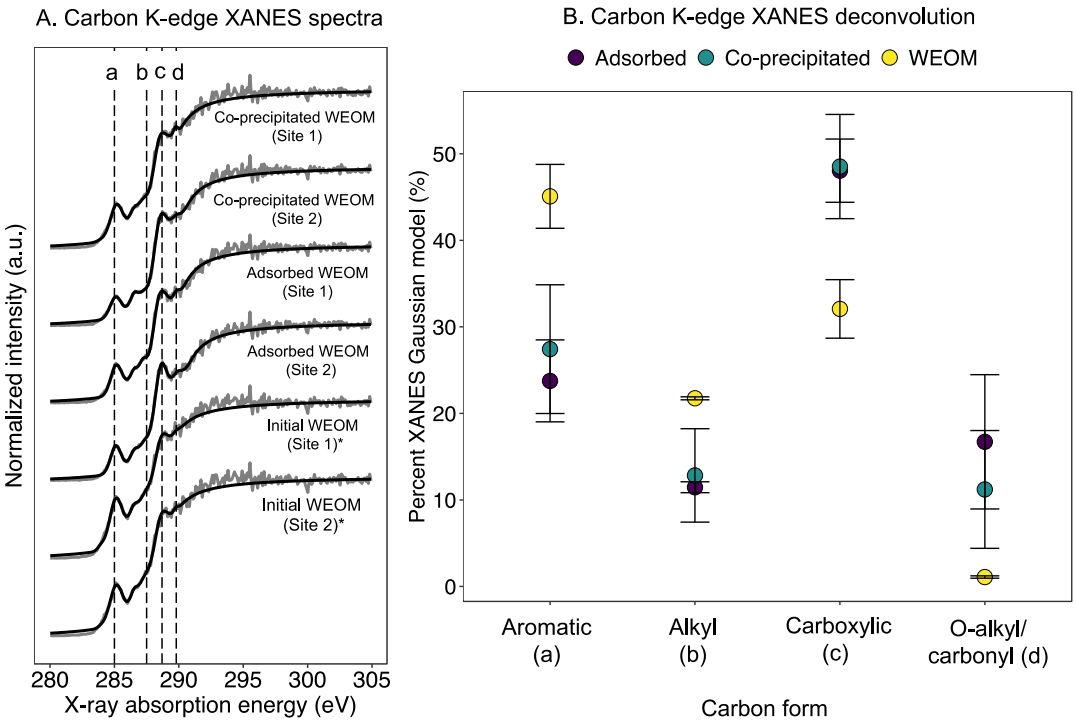

Fig. 1. **A**. Normalized carbon (C) K-edge near-edge X-ray absorption fine structure (XANES) spectra for source (Site 1 and Site 2) water extractable organic matter (WEOM), co-precipitated WEOM-Fe, and adsorbed WEOM-Fe. Lines a, b, c, and d indicate spectral features at ~ 285.0, 287.5, 288.7, and 289.8 eV, corresponding to aromatic, aliphatic, carboxylic, and O-alkyl/carbonyl C functional groups, respectively (Supplementary Table A3.1). **B**. Changes in the relative contribution of C functional groups to the C K-edge XANES Gaussian deconvolution model. Composition values for both sources of WEOM are averaged (±standard deviation). The primary shift in composition between source WEOM and both co-precipitated and adsorbed WEOM-Fe samples is a loss of aromatic groups, enrichment of carboxylic groups, and slight enrichment of O-alkyl/carboxyl groups. Spectra marked with (*) are included in Possinger et al. (2020a).

(i.e., >288 eV) in the lower-energy component was more pronounced with co-precipitated WEOM-Fe relative to adsorbed WEOM-Fe (Fig. 4A). Overall, the higher-energy component was similar between adsorbed and co-precipitated WEOM-Fe (Fig. 4B).

3.2.5. Spatial correlations

The pixel intensity of total C, total Fe, and C and Fe MCR component maps was used to assess the distribution of C and Fe forms. When a reduced Fe(II) component was not detected, only spatial relationships between C forms and total Fe were used. For adsorbed WEOM-Fe (n = 2 images) and co-precipitated WEOM-Fe with no resolved reduced Fe(II) component (n = 3 images), the lower-energy (e.g., aromatic) C component was generally positively correlated with total Fe (Supplementary Fig. A3.13). However, for co-precipitated WEOM-Fe with a resolved Fe(II) component (n = 2 images), both lower-energy C and total C were consistently positively correlated with reduced Fe(II) only (Supplementary Fig. A3.13).

The spatial association between lower-energy C and reduced Fe(II) was highest ($\rho = 0.21$) for the highest resolution co-precipitate measurement (Fig. 5). Line profiles of Fe and C components identified in this image further refine spatial associations between Fe(II) and C forms (Fig. 6). Across the line transect, pixel intensities of reduced Fe(II) and lower-energy C were coupled overall. However, higher-energy C was relatively enriched directly at the boundary of the oxidized Fe(III) cluster (Fig. 6).

4. DISCUSSION

4.1. Coupled carbon and iron transformations in co-precipitated WEOM-Fe

4.1.1. Changes to Fe composition and spatial distribution

The decrease in size and extent of Fe clusters with co-precipitation provides additional visual evidence at single nanometer-scale resolution for changes to Fe structure that was detected using bulk characterization approaches (this study; Mikutta et al., 2010; Mikutta, 2011; Chen et al., 2014; Chen et al., 2016). In this work, we also detected increased subtle contributions of Fe-organic bonding in bulk XAS measurements, consistent with work showing Fe-organic bonds in co-precipitates as C:Fe ratio increased (Chen et al., 2014; Chen et al., 2016). The increased contribution of Fe-organic complexes in co-precipitates was also supported by Mössbauer spectroscopy analysis (Eusterhues et al., 2008) and in-depth EXAFS shell-fitting procedures (Chen et al., 2016). In addition to these expected changes

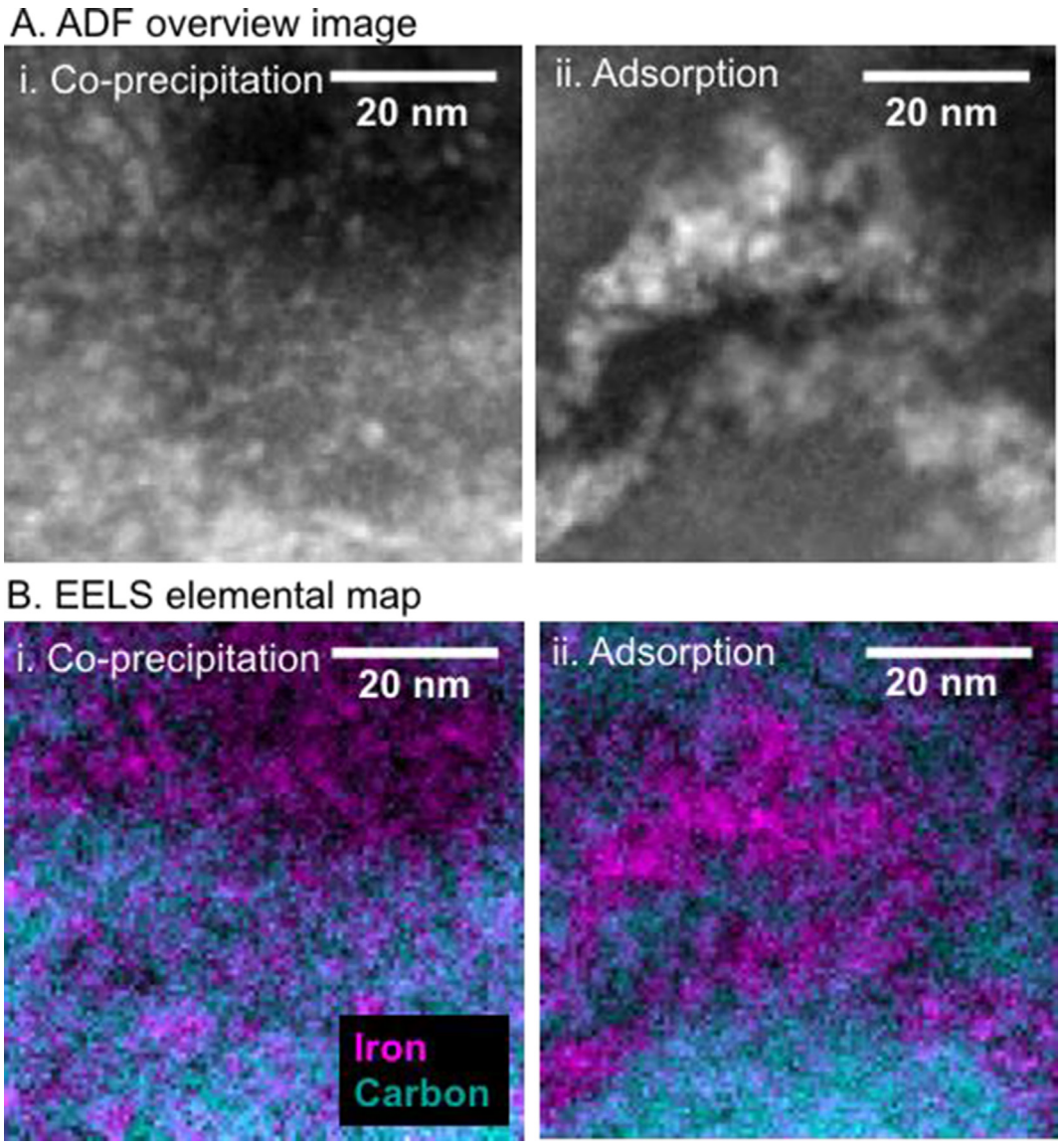

Fig. 2. Overview scanning transmission electron microscopy (STEM) annular dark field (ADF) image (**A**) and electron energy loss spectroscopy (EELS) elemental map (**B**) of co-precipitated and adsorbed water-extractable organic matter (WEOM)-iron (Fe), showing a pattern of chain-like secondary aggregation for adsorption and dispersion of smaller Fe aggregates for co-precipitation.

in bulk Fe composition, the single nm-scale resolution of cryo-STEM-EELS measurements allowed for identification of local Fe(II) reduction in regions of the co-precipitated WEOM-Fe (Fig. 5, Supplementary Fig. A3.12). While studies have previously detected more reduced Fe(II) with co-precipitation in redox-active model systems (Mikutta, 2011), this change has not been consistently detected in co-precipitation studies, particularly in experiments using natural OM sources (Eusterhues et al., 2008; Chen et al., 2014; Chen et al., 2016). The co-occurrence of aromatic-rich organic C with reduced Fe(II) highlights the role of divergent WEOM composition to influence the extent of Fe reduction during co-precipitation (Mikutta, 2011). Therefore, further experiments testing WEOM mixtures with increasing contributions of redox-active constituents would enable better prediction of Fe reduction potential during co-precipitation.

4.1.2. Changes to C composition and spatial distribution

While differences in Fe structure and chemistry between co-precipitation and adsorption are expected, the degree of alteration of C compared to the initial OM source as a result of co-precipitation remains a critical question for understanding potential changes in co-precipitated OM bioavailability. In this study, a two-fold decrease in aromatic C signal compared to original WEOM was observed for both co-precipitated and adsorbed samples using bulk spectroscopic characterization (Fig. 1, Supplementary Table A4.2). Exclusion of aromatic WEOM constituents confirms that co-precipitation is not exclusively a non-selective physical occlusion process (Kleber et al., 2015). Moreover, using high-resolution mapping of C composition, we detected distinct spatial patterns of lower- and higher-energy C components (Supplementary Fig. A3.12, Figs. 5 and 6) (hereafter referred to as "aromatic" and

Table 2
Elemental spatial correlations among iron (Fe), carbon (C), nitrogen (N), and oxygen (O) derived from scanning transmission electron microscopy-electron energy loss spectroscopy (STEM-EELS) elemental maps. Replicate images are associated with co-precipitated or adsorbed samples from either Site 1 or Site 2-sourced water-extractable organic matter (WEOM).

Pair	C-Fe		C-N		Fe-N		Fe-O	
Treatment	Adsorbed	Co-precipitated	Adsorbed	Co-precipitated	Adsorbed	Co-precipitated	Adsorbed	Co-precipitated
Images (N)	7	8	5	3	5	3	5	3
WEOM sources	Site 1 and 2	Site 1 and 2	Site 1	Site 1	Site 1	Site 1	Site 1	Site 1
Average Spearman's ρ	−0.26	−0.06	0.03	0.00	−0.03	0.00	0.18	0.13
± Standard deviation	(0.25)	(0.14)	(0.04)	(0.17)	(0.03)	(0.03)	(0.16)	(0.12)

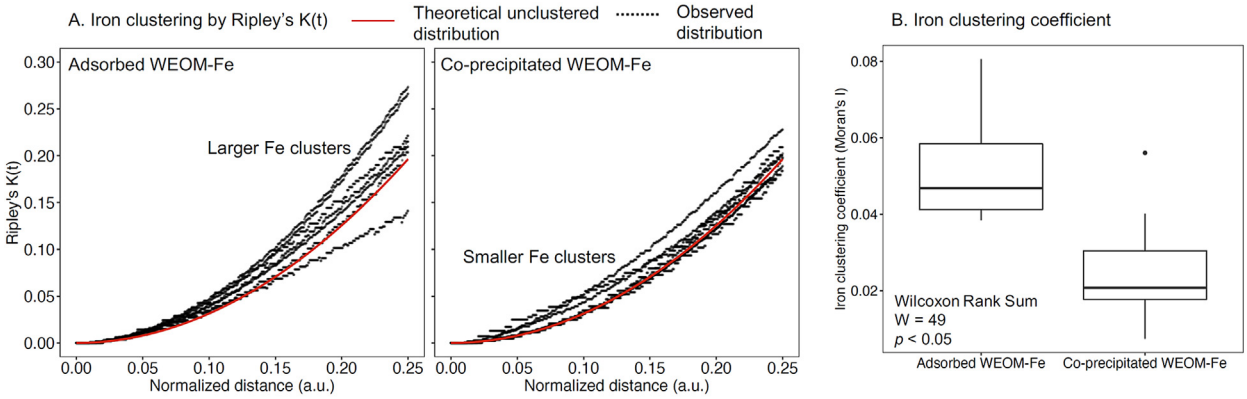

Fig. 3. **A**. Spatial quantification of iron (Fe) clustering in co-precipitated and adsorbed water extractable organic matter (WEOM)-Fe samples. Ripley's K(t) is shown as a function of normalized distance from each randomly sampled Fe point in a spatial point pattern for each image (n = 8 images for co-precipitation and n = 7 images for adsorption, shown by individual black dotted lines). Overall greater clustering and larger clusters were detected for adsorbed WEOM-Fe, indicated by the observed distributions above the theoretical distribution (red line) at larger distances. **B**. Median (boxplot line) Fe clustering coefficients (Moran's I parameter) for adsorbed and co-precipitated WEOM-Fe images. Lower and upper edges of boxes show first and third quartiles (25th and 75th percentiles) and lower and upper whiskers show the smallest and largest value no further than 1.5*interquartile range (IQR) of the box edges. Individual points beyond whiskers are considered outliers.

"oxidized" C for simplicity). The detection of overall aromatic C and reduced Fe(II) co-location and enrichment of oxidized C at the oxidized Fe(III) boundary does not support the presence of unaltered patches of occluded source OM. These spatial associations also suggest that co-precipitated OM is directly altered relative to its source composition by Fe-organic interaction mechanisms (e.g., Fe (II or III)-organic complex formation and surface adsorption), also suggested by Kleber et al. (2015) in addition to physical occlusion.

The distribution of C and Fe forms across the ~ 40x40 nm field of view (Fig. 5) in combination with a finer-scale line profile (Fig. 6) points towards a distinct proposed spatial arrangement of C within co-precipitates (Fig. 7). At the whole-image scale (Fig. 5), oxidized Fe(III) was loosely clustered (lacking distinctive ferrihydrite chain-like aggregation) into C-free regions, resulting in a spatial separation of aromatic C from oxidized Fe(III). In contrast, reduced Fe(II) and aromatic C were spatially co-located in the spaces between oxidized Fe(III) aggregations. When viewed as a high-resolution transect, the enrichment of oxidized C at the oxidized Fe(III) interface becomes detectable (Fig. 6). This relationship is supported by the weak (ρ = 0.09) but statistically significant spatial correlation between oxidized C and oxidized Fe(III) at the whole-image scale (Fig. 5). Together, the spatial separation of aromatic C from oxidized Fe(III) on the larger scale and the spatial association of oxidized C with oxidized Fe(III) at the finer scale points to a gradient of C composition as a function of distance from the center of unstructured oxidized Fe(III) aggregates (Fig. 7).

4.1.3. Organo-iron redox reactions

The observed spatial associations between lower-energy C and Fe(II) EELS components point towards Fe(III) reduction via substituted aromatic C-Fe interactions during co-precipitation. For example, at a high C:Fe ratio (as used in this study), C in excess of Fe could facilitate soluble Fe complexation, either as Fe(III) or in redox-coupled complexation as Fe(II) (Bhattacharrya et al., 2019). The observed energy shifts in bulk Fe XANES are also consistent with increased contribution of organically-complexed Fe (Supplementary Fig. A3.9). Many organic functional groups linked to abiotic Fe reduction are present in the ~ 284–286.5 eV region, including substituted aromatic groups associated with phenolic compounds (Solomon

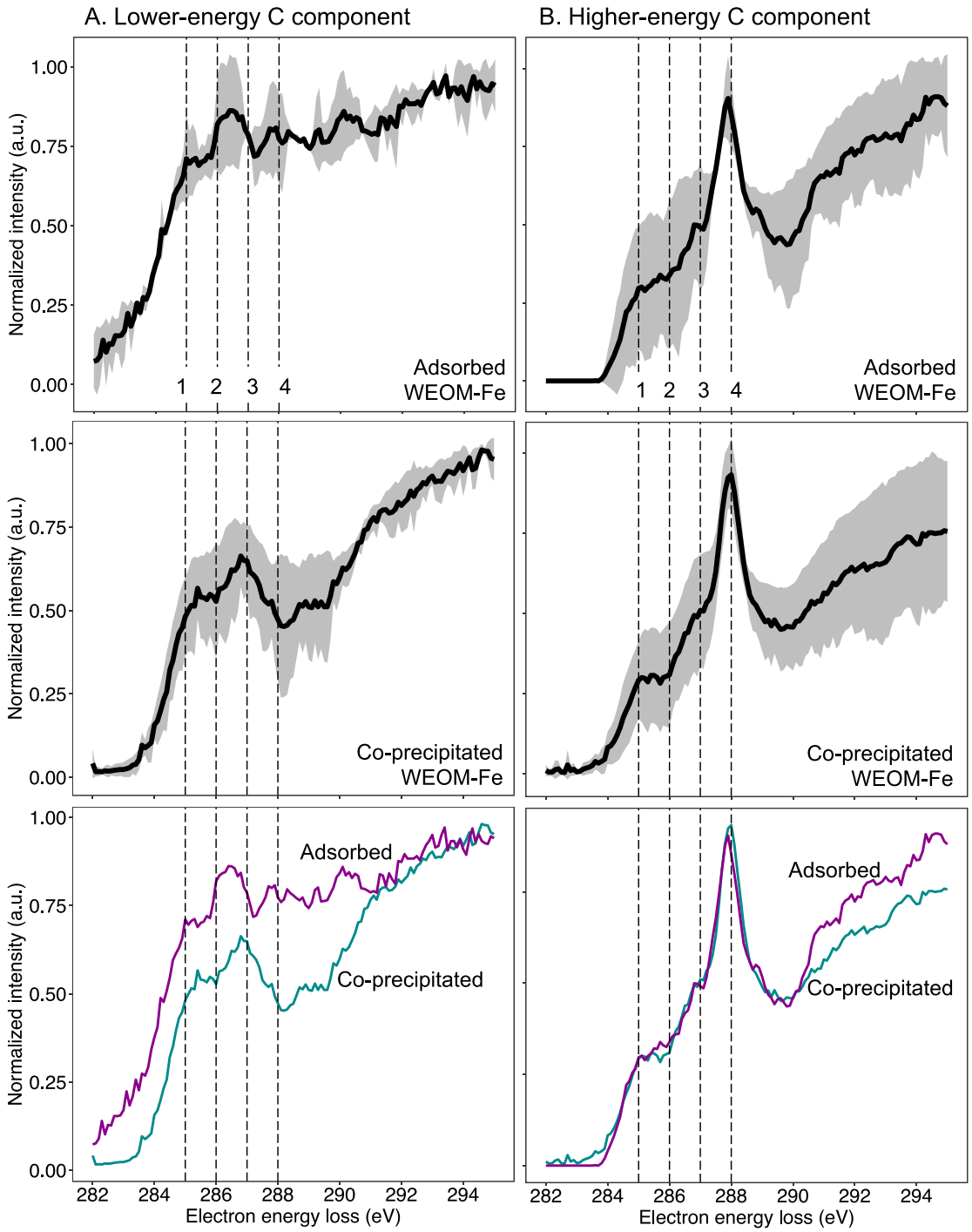

Fig. 4. Carbon (C) K-edge electron energy loss spectroscopy (EELS) multivariate curve resolution (MCR) outputs for adsorbed or co-precipitated water-extractable organic matter (WEOM)-iron (Fe) image maps. Spectra are grouped by the lower-energy (**A**) and higher-energy (**B**) MCR components. The average spectrum (black line) with standard deviation (grey shaded region) is shown (n = 2 images for adsorbed and n = 5 images for co-precipitated WEOM-Fe). Lines 1–4 indicate 285.0, 286.0, 287.0, and 288.0 eV energy positions, respectively. For all MCR outputs, values are constrained to counts > 0.

et al., 2009). In model-system co-precipitation experiments, abiotic mineralization of the catechol constitutent in 3,4-hydroxybenzoic acid was linked with Fe reduction in ferrihydrite (Mikutta, 2011). Phenol reduction of Fe(III) to Fe(II) and complexation of Fe(II) has also been linked with slower precipitation of Fe in high OM peatlands (Wan et al., 2018) and during DOM flocculation (Nierop et al., 2002). Additionally, substituted aromatic C

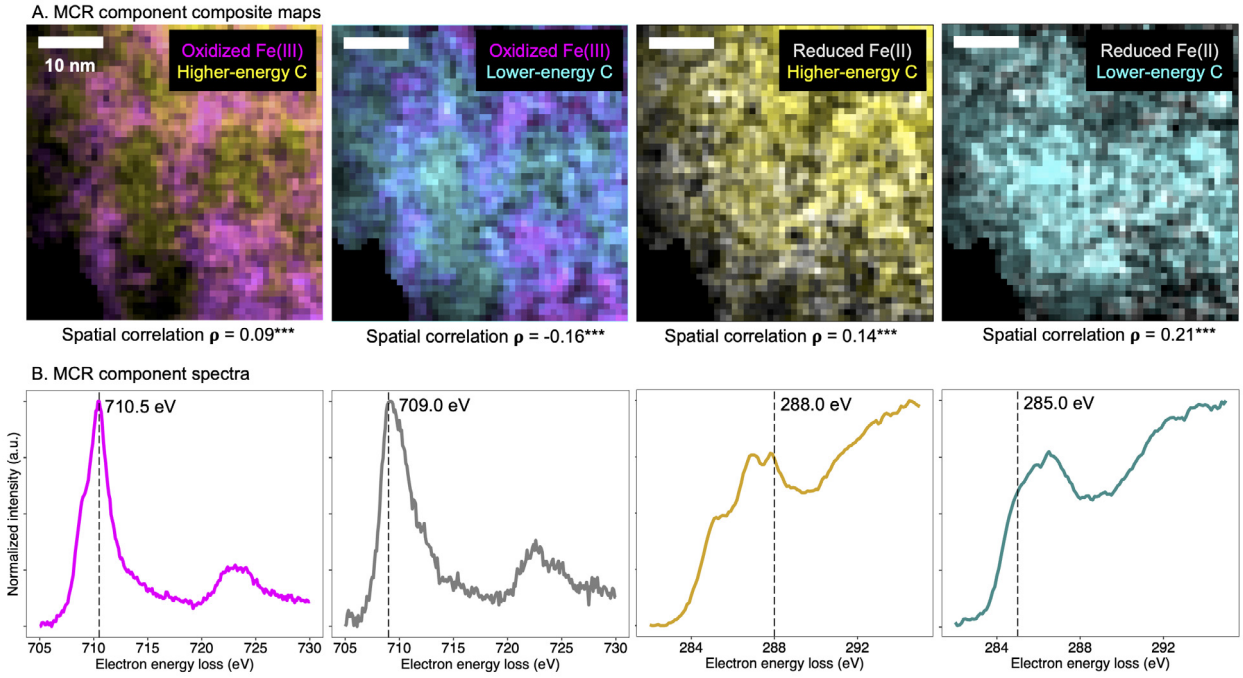

Fig. 5. Carbon (C) K-edge and iron (Fe) $L_{2,3}$-edge electron energy loss spectroscopy (EELS) multivariate curve resolution (MCR) output composite maps (**A**) and spectra (**B**) for an example high-resolution co-precipitated WEOM-Fe image. Data are shown for measurement "i" in Supplementary Table A4.4. In composite images (**A**), 1 pixel ~ 0.9 nm. In **B**, spectra are shown normalized (maximum intensity = 1). Vertical lines are shown as reference for major spectrum features: the highest expected Fe $L_{2,3}$-edge oxidation state at 710.5 eV (used as reference energy) (Gloter et al., 2004), a lower-energy shift representative of reduced Fe(II) at 709.0 eV, higher energy (more oxidized) C at > 288.0 eV, and lower-energy (more reduced/aromatic) C at ~ 285.0 eV.

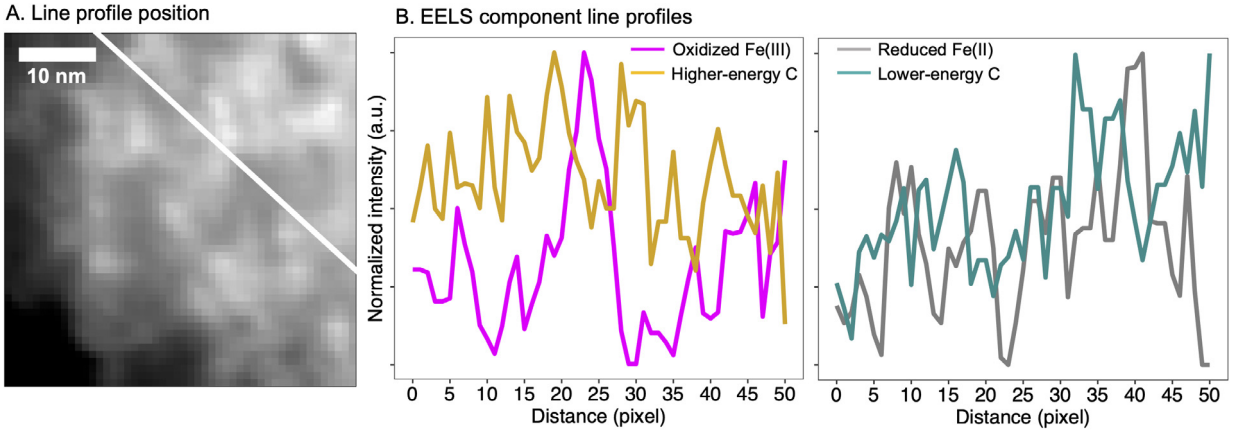

Fig. 6. Carbon (C) K-edge and iron (Fe) $L_{2,3}$-edge electron energy loss spectroscopy (EELS) overview annual dark field (ADF) image (**A**) and multivariate curve resolution (MCR) output line profiles (**B**) for an example high-resolution co-precipitated WEOM-Fe image. **A.** In the ADF overview image, brighter spots indicate areas of loosely-clustered small Fe aggregates (1–5 nm in size). The white line indicates the location of the line profile measurements. **B**. Line profiles show variation in MCR output components normalized (maximum = 1) across the line profile (spectra and composite maps in Fig. 5).

functional groups have been linked with promotion of biotic Fe reduction through extracellular electron transfer, in both highly aromatic materials such as pyrogenic organic matter (Sun et al., 2018) and as a component of natural OM in soil and water (Uchimiya and Stone, 2009). However, experiments to track redox changes over time (using both wet-chemical and spectroscopic approaches), to assess possible contribution of biotic reduction, and to assess the role of initial C:Fe ratio are necessary to further interrogate the mechanism of Fe(III) reduction in these systems. While our results do not directly probe the mechanism of these organo-Fe redox reactions, they provide

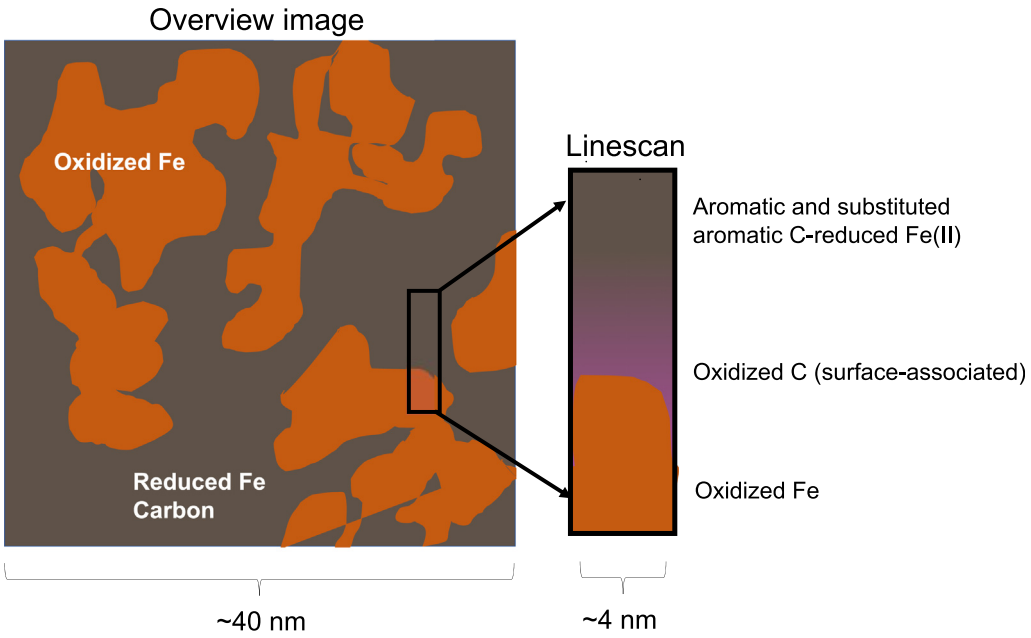

Fig. 7. Simplified schematic of proposed spatial distribution of co-precipitate carbon (C) and iron (Fe) forms based on scanning transmission electron microscopy-electron energy loss spectroscopy (STEM-EELS) and bulk X-ray spectroscopy characterization. Oxidized Fe is loosely aggregated and largely separate from C on the 40x40 nm scale (taken from Fig. 5), but spatial association between higher-energy oxidized C and oxidized Fe at the nm scale points to a gradient of C forms as a function of distance from the oxidized Fe(III) interface (taken from Fig. 6).

incentive for further evaluation of how substituted aromatic C composition of natural OM influences the degree of Fe reduction during co-precipitation (Mikutta, 2011).

4.2. Environmental relevance

While changes to Fe and C composition were local and spatially heterogeneous, reduced Fe(II)-aromatic C accounted for approximately 50% of the sample image in the reduced regions (Fig. 5). This direct evidence of substantial OM-Fe redox transformations in local co-precipitate environments provides a possible mechanism for observations of higher WEOM bioavailability and reactivity in co-precipitates, together with properties such as higher reactive surface area, mineral structural defects, and greater proportion of complexed vs. surface-adsorbed WEOM (Mikutta, 2011; Eusterhues et al., 2014; Mikutta et al., 2014). Iron-facilitated SOM oxidation may also result in direct abiotic OM mineralization to carbon dioxide (CO_2), in addition to effects on C composition. For example, hydroquinone-facilitated pathways may generate reactive intermediates for Fenton reactions involved in abiotic OM oxidation (Contreras et al., 2011; Wan et al., 2018), which may significantly contribute to total soil CO_2 emissions in some systems (Yu and Kuzyakov, 2021). In addition to previously observed increases in Fe reactivity due to disaggregated Fe distribution (Eusterhues et al., 2014), the increased presence of Fe(II) may also influence Fe oxide transformation. While soluble Fe(II) on ferrihydrite surfaces is a known driver of faster crystallization rate (Hansel et al., 2005; Yee et al., 2006), the detected Fe(II) was likely present as a Fe(II)-organic complex in this study, complicating the potential influence of increased Fe(II) on ferrihydrite transformation.

In this study, co-precipitation of C in excess of Fe (at a 10:1 molar ratio) is most representative of the interface between organic and mineral horizons in organic soils, sediments, wetland soils, and other environments with high OM and low pedogenic Fe, low Fe solubility, or Fe depletion on an environmental scale. However, C in excess of Fe may also occur on the scale of interactions between organic macromolecules, microbial cells, and soluble Fe phases (e.g., in the rhizosphere) (Lemanceau et al., 2009). As such, predicting the environmental impact of co-precipitation processes would be informed by experiments modeling the conditions and reagents present across the spectrum of high C:Fe co-precipitation pathways.

5. CONCLUSIONS

Using spatially-resolved, high-resolution STEM-EELS measurements in conjunction with bulk spectroscopic analyses, we demonstrate changes to both Fe and C composition with co-precipitation compared to adsorption, including: (1) less Fe aggregation, (2) increased Fe(II) and Fe-organic bonding, (3) the presence of spatially-distinct aromatic and oxidized C forms, and (4) the overall spatial association of aromatic (and/or substituted aromatic) C forms with Fe(II). Therefore, co-precipitation constitutes not merely a physical encapsulation without interaction between C and Fe, but possibly causes bi-directional C-Fe reactions. These results also suggest that the primary distinction between co-precipitation and adsorption is not the degree of physical occlusion, but the extent of complex

formation and abiotic reduction processes, where C forms play a major role. Consideration of co-precipitation processes and their environmental relevance should consequently focus on the parameters influencing abiotic reduction, such as the relative differences in redox-active substituted aromatic functional groups in source OM (e.g., in phenolic compounds). We would therefore expect co-precipitation reactions to differ between different ecosystems if OM properties vary in their redox-active C forms. These processes may be relevant not only for accumulation of OM from a soil C sequestration perspective, but also for contaminant transformation, water treatment, and coupled C-Fe biogeochemical cycling. Therefore, future studies should evaluate the effect of varying redox-active compound composition of OM, as well as environmental redox drivers, on the characteristics of co-precipitates in different ecosystems and engineered systems, particularly at oxic-anoxic interfaces with high OM input.

DATA REPOSITORY

Research data associated with this article are accessible via the Cornell University eCommons repository (https://doi.org/10.7298/6134-h423).

Declaration of Competing Interest

The authors declare that they have no known competing financial interests or personal relationships that could have appeared to influence the work reported in this paper.

ACKNOWLEDGEMENTS

Funding for this study was provided by the NSF IGERT in Cross-Scale Biogeochemistry and Climate at Cornell University (NSF Award #1069193) and the Technical University of Munich Institute for Advanced Studies. Additional research funds were provided by the Andrew W. Mellon Foundation and the Cornell College of Agriculture and Life Sciences Alumni Foundation. M.J.Z. and L.F.K. acknowledge support by the NSF (DMR-1654596) and Packard Foundation. This work uses research conducted at the Cornell High Energy Synchrotron Source (CHESS) which is supported by the National Science Foundation under award DMR-1332208. The Cornell Center for Materials Research (CCMR) is funded by NSF MRSEC (DMR-1719875). Research described in this paper was performed at the Canadian Light Source (CLS), which is supported by the Canada Foundation for Innovation, Natural Sciences and Engineering Research Council of Canada, the University of Saskatchewan, the Government of Saskatchewan, Western Economic Diversification Canada, the National Research Council Canada, and the Canadian Institutes of Health Research. The authors also thank John Grazul and Malcolm Thomas of the CCMR facility, Rong Huang of CHESS, and Kelly Hanley and Akio Enders of Cornell University for technical assistance.

APPENDIX A. SUPPLEMENTARY MATERIAL

Supplementary data to this article can be found online at https://doi.org/10.1016/j.gca.2021.09.003.

REFERENCES

Baek D. J., Lu D., Hikika Y., Hwang H. Y. and Kourkoutis L. F. (2016) Ultrathin epitaxial barrier layer to avoid thermally induced phase transformation in oxide heterostructures. *ACS Appl. Mater. Interfaces* **9**, 54–59.

Bailey S. W., Brousseau P. A., McGuire K. J. and Ross D. S. (2014) Influence of landscape position and transient water table on soil development and carbon distribution in a steep, headwater catchment. *Geoderma* **226–227**, 279–289.

Berry A. J., O'Neill H., St C., Jayasuriya K. D., Campbell S. J. and Foran G. J. (2003) XANES calibrations for the oxidation state of iron in silicate glass. *Am. Mineral.* **88**(7), 967–977.

Bhattacharyya A., Schmidt M. P., Stavitski E., Asimzadeh B. and Martínez C. E. (2019) Ligands representing important functional groups of natural organic matter facilitate Fe redox transformations and resulting binding environments. *Geochem. Cosmochim. Acta* **251**, 157–175.

Camp C. H. (2019) PyMCR: a Python library for multivariate curve resolution analysis with alternating regression (mcr-Ar). *J. Res. Natl. Inst. Stan.* **124**.

Chen C., Dynes J. J., Wang J. and Sparks D. L. (2014) Properties of Fe-organic matter associations via coprecipitation versus adsorption. *Environ. Sci. Technol.* **48**, 13751–13759.

Chen K., Chen T., Chan Y., Cheng C., Tzou Y., Liu Y. and Teah H. (2016) Stabilization of natural organic matter by short-range-order iron hydroxides. *Environ. Sci. Technol.* **50**, 12612–12620.

Collignon C. and Rangerand Turpault M. P. (2012) Seasonal dynamics of Al- and Fe-bearing secondary minerals in an acid forest soil: influence of Norway spruce roots (Picea abies (L.) Karst.). *Eur. J. Soil Sci.* **63**, 592–602.

Contreras D., Rodríguez J., Basaez L., Freer J., Valenzuela R., Mansilla H. and Vanysek P. (2011) New insights in the dihydroxybenzenes-driven Fenton reaction: electrochemical study of interaction between dihydroxybenzenes and Fe(III). *Water Sci Technol.* **64**(10), 2101–2108.

Deng Y. and Dixon J. B. (2002) Soil organic matter and organic-mineral interactions. In *Soil Mineralogy with Environmental Applications, SSSA Book Series 7* (eds. J. B. Dixon and D. G. Shulze). Soil Science Society of America Inc, Madison, WI, pp. 69–108.

Eusterhues K., Hadrich A., Neidhardt J., Kusel K., Keller T. F., Jandt K. D. and Totsche K. U. (2014) Reduction of ferrihydrite with adsorbed and coprecipitated organic matter: microbial reduction by *Geobacter bremensis* versus abiotic reduction by Na-dithionite. *Biogeosci. Discuss.* **11**, 6039–6067.

Eusterhues K., Rennert T., Knicker H., Kögel-Knabner I., Totsche K. U. and Schwertmann U. (2011) Fractionation of organic matter due to reaction with ferrihydrite: coprecipitation versus adsorption. *Environ. Sci. Technol.* **45**, 527–533.

Eusterhues K., Wagner F. E., Häusler W., Hanzik M., Knicker H., Totsche K. U., Kögel-Knabner I. and Schwertmann U. (2008) Characterization of ferrihydrite-soil organic matter co-precipitates by X-ray diffraction and Mössbauer spectroscopy. *Environ. Sci. Technol.* **42**(21), 7891–7897.

Fritzche A., Schröder C., Wieczorek A. K., Händel M., Ritschel T. and Totsche K. U. (2015) Structure and composition of Fe-OM co-precipitates that form in soil-derived solutions. *Geochim. Cosmochim. Acta* **169**, 167–183.

Ginn B., Meile C., Wilmoth J., Tang Y. and Thompson A. (2017) Rapid iron reduction rates are stimulated by high-amplitude redox fluctuations in a tropical forest soil. *Environ. Sci. Technol.* **51**(6), 3250–3259.

Gloter A., Zbinden M., Guyot F., Gaill F. and Colliex C. (2004) TEM-EELS study of natural ferrihydrite from geological-

biological interactions in hydrothermal systems. *Earth Planet. Sci. Lett.* **222**(3–4), 947–957.
Hansel C. M., Benner S. G. and Fendorf S. (2005) Competing Fe (II)-induced mineralization pathways of ferrihydrite. *Environ. Sci. Technol.* **39**, 7147–7153.
Henneberry Y. K., Kraus E. C., Nico P. S. and Horwath W. R. (2012) Structural stability of coprecipitated natural organic matter and ferric iron under reducing conditions. *Org. Geochem.* **48**, 81–89.
Hestrin R., Torres-Rojas D., Dynes J. J., Hook J. M., Regier T. Z., Gillespie A. W., Smernik R. J. and Lehmann J. (2019) Fire-derived organic matter retains ammonia through covalent bond formation. *Nat. Commun.* **10**, 664.
Heymann K., Lehmann J., Solomon D., Schmidt M. W. I. and Regier T. (2011) C 1s K-edge near edge X-ray absorption fine structure (NEXAFS) spectroscopy for characterizing functional group chemistry of black carbon. *Org. Geochem.* **42**(9), 1055–1064.
Inagaki T. M., Possinger A. R., Grant K. E., Schweizer S. A., Mueller C. W., Derry L. A., Lehmann J. and Kögel-Knabner I. (2020) Subsoil organo-mineral associations under contrasting climate conditions. *Geochim. Cosmochim. Acta* **270**, 244–263.
Lehmann J. and Kleber M. (2015) The contentious nature of soil organic matter. *Nature* **528**, 60–68.
Lemanceau P., Bauer P., Kraemer S. and Briat J.-F. (2009) Iron dynamics in the rhizosphere as a case study for analyzing interactions between soils, plants, and microbes. *Plant Soil* **321**, 513–535.
Kleber M., Eusterhues K., Keiluweit M., Mikutta C., Mikutta R. and Nico P. S. (2015) Mineral-organic associations: formation, properties, and relevance in soil environments. *Adv. Agron.* **130**, 1–140.
Kourkoutis L. F., Plitzko J. M. and Baumeister W. (2012) Electron microscopy of biological materials at the nanometer scale. *Annu. Rev. Mater. Res.* **42**, 33–58.
Mikutta C. (2011) X-ray absorption spectroscopy study on the effect of hydroxybenzoic acids on the formation and structure of ferrihydrite. *Geochim. Cosmochim. Acta* **75**, 5122–5139.
Mikutta C., Frommer J., Voegelin A., Kaegi R. and Kretzschmar R. (2010) Effect of citrate on the local Fe coordination in ferrihydrite, arsenate binding, and ternary arsenate complex formation. *Geochim. Cosmochim. Acta* **74**, 5574–5592.
Mikutta R., Lorenz D., Guggenberger G., Haumaier L. and Freund A. (2014) Properties and reactivity of Fe-organic matter associations formed by coprecipitation versus adsorption: Clues from arsenate batch adsorption. *Geochim. Cosmochim. Acta* **144**, 258–276.
Miot J., Benzerara K. and Kappler A. (2014) Investigating microbe-mineral interactions: recent advances in X-ray and electron microscopy and redox-sensitive methods. *Annu. Rev. Earth Planet. Sci.* **42**, 271–289.
Mundy J. A., Hikita Y., Hidaka T., Yajima T., Higuchi T., Hwang H. Y., Muller D. A. and Kourkoutis L. F. (2014) Visualizing the interfacial evolution from charge compensation to metallic screening across the manganite metal-insulator transition. *Nat. Commun.* **5**, 3464.
Nierop K. G. J. J., Jansen B. and Verstraten J. M. (2002) Dissolved organic matter, aluminum, and iron interactions: precipitation induced by metal/carbon ratio, pH, and competition. *Sci. Total Environ.* **300**(1–3), 201–211.
Possinger A. R., Bailey S. W., Inagaki T. M., Kögel-Knabner I., Dynes J. J., Arthur Z. A. and Lehmann J. (2020a) Organo-mineral interactions and soil carbon mineralizability with variable saturation cycle frequency. *Geoderma* **375** 114883.
Possinger A. R., Zachman M. J., Enders A., Levin B. D. A., Muller D. A., Kourkoutis L. F. and Lehmann J. (2020b) Organo-organic and organo-mineral interfaces in soil at the nanometer scale. *Nat. Commun.* **11**, 6103.
Prietzel J., Thieme J., Eusterhues K. and Eichert D. (2007) Iron speciation in soils and soil aggregates by synchrotron-based X-ray microspectroscopy (XANES, μ-XANES). *Eur. J. Soil Sci.* **58**, 1027–1041.
Ravel B. and Newville M. (2005) Athena, artemis, hephaestus: data analysis for X-ray absorption spectroscopy using IFEFFIT. *J. Synchrotron Rad.* **12**, 537–541.
RStudio Team (2015) *RStudio: Integrated Development for R.* RStudio Inc, Boston, URL http://www.rstudio.com/.
R Core Team (2019) *R: A language and environment for statistical computing.* R Foundation for Statistical Computing, Vienna, Austria, https://www.R-project.org/.
Schmidt M. W. I., Torn M. S., Abiven S., Dittmar T., Guggenberger G., Janssens I. A., Kleber M., Kögel-Knabner I., Lehmann J., Manning D. A. C., Nannipieri P., Rasse D. P., Weiner S. and Trumbore S. E. (2011) Persistence of soil organic matter as an ecosystem property. *Nature* **478**(7367), 49–56.
Schneider C. A., Rasband W. S. and Eliceiri K. W. (2012) NIH Image to ImageJ: 25 years of image analysis. *Nat. Methods* **9**(7), 671–675.
Schwertmann U. and Cornell R. M. (2000) *Iron Oxides in the Laboratory: Preparation and Characterization*, 2nd Edition. Wiley-VCG Verlag GmbH, Weinheim, DE.
Schwertmann U. and Taylor R. M. (1989) Iron oxides. In *Minerals in Soil Environments* (eds. J. B. Dixon and S. B. Weed), 2nd Edition. Soil Science Society of America Inc, Madison, WI, pp. 379–438.
Shimizu M., Zhou J. H., Schroder C., Obst M., Kappler A. and Borch T. (2013) Dissimilatory reduction and transformation of ferrihydrite-humic acid coprecipitates. *Environ. Sci. Technol.* **47**, 13375–13384.
Solomon D., Lehmann J., Kinyangi J., Liang B., Heymann K., Dathe L., Hanley K., Wirick S. and Jacobsen C. (2009) Carbon (1s) NEXAFS spectroscopy of biogeochemically relevant reference organic compounds. *Soil Sci. Soc. Am. J.* **73**, 1817–1830.
Sun T., Levin B. D. A., Schmidt M. P., Guzman J. J. L., Enders A., Martínez C. E., Muller D. A., Angenent L. T. and Lehmann J. (2018) Simultaneous quantification of electron transfer by carbon matrices and functional groups in pyrogenic carbon. *Environ. Sci. Technol.* **52**(15), 8538–8547.
Thompson A., Chadwick O. A., Rancourt D. G. and Chorover J. (2006) Iron-oxide crystallinity increases during soil redox oscillations. *Geochim. Cosmochim. Acta* **70**, 1710–1727.
Uchimiya M. and Stone A. T. (2009) Reversible redox chemistry of quinones: Impact on biogeochemical cycles. *Chemosphere* **77**(4), 451–458.
Vilge-Ritter A., Rose J., Masion A., Bottero J. Y. and Laine J. M. (1999) Chemistry and structure of aggregates formed with Fe-salts and natural organic matter. *Colloids Surf. A* **147**, 297–308.
Wan X., Xiang W., Wan N., Yan S., Bao Z. and Wang Y. (2018) Complexation and reduction of iron by phenolic substances: Implications for transport of dissolved Fe from peatlands to aquatic ecosystems and global iron cycling. *Chem. Geol.* **298**, 128–138.
Westre T. E., Kennepohl P., DeWitt J. G., Hedman B., Hodgson K. O. and Solomon E. I. (1997) A multiplet analysis of Fe K-edge 1s 3d pre edge features of iron complexes. *J. Am. Chem. Soc.* **119**, 6297–6314.
Wojdyr M. (2010) Fityk: a general-purpose peak fitting program. *J. Appl. Cryst.* **43**, 1126–1128.
Yee N., Shaw S., Benning L. G. and Nguyen T. H. (2006) The rate of ferrihydrite transformation to goethite via the Fe(II) pathway. *Am. Mineral.* **91**, 92–96.

Yu G.-H. and Kuzyakov Y. (2021) Fenton chemistry and reactive oxygen species in soil: Abiotic mechanisms of biotic processes, controls, and consequences for carbon and nutrient cycling. *Earth-Sci. Rev.* **214** 103525.

Zachman M. J., Tu Z., Choudhury S., Archer L. A. and Kourkoutis L. F. (2018) Cryo-STEM mapping of solid-liquid interfaces and dendrites in lithium-metal batteries. *Nature* **560**, 345–349.

Associate editor: Juan Liu